applied sciences

MDPI

Article

Accelerometer-Based Pavement Classification for Vehicle Dynamics Analysis Using Neural Networks

Vytenis Surblys [1], Edward Kozłowski [2,*], Jonas Matijošius [3], Paweł Gołda [4], Agnieszka Laskowska [2] and Artūras Kilikevičius [3]

[1] Department of Automobile Engineering, Vilnius Gediminas Technical University, Plytinės Str. 25, LT-10105 Vilnius, Lithuania; vytenis.surblys@vilniustech.lt
[2] Faculty of Management, Lublin University of Technology, Nadbystrzycka 38, 20-618 Lublin, Poland; a.laskowska@pollub.pl
[3] Mechanical Science Institute, Vilnius Gediminas Technical University, Plytinės Str. 25, LT-10105 Vilnius, Lithuania; jonas.matijosius@vilniustech.lt (J.M.); arturas.kilikevicius@vilniustech.lt (A.K.)
[4] Faculty of Aviation, Polish Air Force University, Dywizjonu 303 no. 35, 08-521 Dęblin, Poland; p.golda@law.mil.pl
* Correspondence: e.kozlovski@pollub.pl

Abstract: This research examines the influence of various pavement types on vehicle dynamics, specifically concentrating on vertical acceleration and its implications for unsprung mass, including the wheels and suspension system. The objective of this project was to categorize pavement types with accelerometer data, enabling a deeper comprehension of the impact of road surface conditions on vehicle stability, comfort, and mechanical stress. Two categorization methods were utilized: a neural network and a multinomial logistic regression model. Accelerometer data were gathered while a car navigated diverse terrain types, such as grates, potholes, and cobblestones. The neural network model exhibited exceptional performance, with 100% accuracy in categorizing all surface types, while the multinomial logistic regression model reached 97.14% accuracy. The neural network demonstrated exceptional efficacy in differentiating intricate surface types such as potholes and grates, surpassing the logistic regression model which had difficulties with these surfaces. These results underscore the neural network's effectiveness in the real-time categorization of road surfaces, enhancing the comprehension of vehicle dynamics influenced by pavement conditions. Future studies must tackle the difficulty of identifying analogous surfaces by enhancing methodologies or integrating more data attributes for greater precision.

Keywords: vehicle dynamics; pavement classification; accelerometer data; neural networks; road surface monitoring

Citation: Surblys, V.; Kozłowski, E.; Matijošius, J.; Gołda, P.; Laskowska, A.; Kilikevičius, A. Accelerometer-Based Pavement Classification for Vehicle Dynamics Analysis Using Neural Networks. *Appl. Sci.* **2024**, *14*, 10027. https://doi.org/10.3390/app142110027

Academic Editors: Difei Wu and Hongduo Zhao

Received: 30 September 2024
Revised: 28 October 2024
Accepted: 31 October 2024
Published: 3 November 2024

1. Introduction

Road surface characteristics substantially affect vehicle dynamics, particularly regarding stability and passenger comfort [1]. These attributes are essential for autonomous cars, which require precise and instantaneous data on road conditions to guarantee safe and pleasant operation [2]. Prior research has indicated that accelerometer data analysis may effectively identify road surface imperfections; nonetheless, there is a need for more efficient data processing methodologies [3]. In this context, neural networks integrated with accelerometers provide dependable and precise surface categorization. The objective of this project was to develop and validate a system for the real-time categorization of road surfaces to enhance vehicle stability and comfort.

The impact of surfaces on land vehicle dynamics is a critical study domain [4], particularly concerning vehicle stability [5], suspension system efficacy [6], and passenger comfort [7]. This study demonstrates how varying road surfaces, surface roughness, and

sliding dangers impact cars, while contemporary techniques like accelerometer data processing and numerical models enhance the comprehension of these phenomena.

A previous, significant study introduced the VDMIDL (Vehicle Dynamics Model-Informed Deep Learning) methodology for assessing road surface conditions, integrating vehicle dynamics physics with deep learning models. This method enhances road surface identification, hence refining trajectory planning and decision-making for autonomous cars [8]. This is particularly applicable when conditions become challenging or unforeseen road abnormalities arise that may jeopardize the vehicle's stability [9].

Moreover, previous research investigating vehicle dynamics on uneven bridge surfaces has indicated that road imperfections and the vehicle's velocity may lead to substantial alterations in dynamics, including vibrations and heightened stress on the car's suspension system. This work used finite element methods and line methods for the precise modeling of vehicle–pavement interactions, specifically focusing on the impacts of vehicle suspension stiffness and dampening [10].

A further significant factor addressed in the literature is hydroplaning risk [11–14], which may be alleviated by enhancing road surface roughness, the tire design, and the tread depth. Studies indicate that surface drainage and a reduced fluid layer on the roadway may decrease the likelihood of skidding. Hydroplaning is a perilous condition in which a film of water between the tires and the roadway results in a lack of grip. This underscores the significance of surface roughness and pavement quality, particularly in rainy situations.

The literature also emphasizes the impact of potholes and other surface abnormalities on vehicle dynamics [15,16]. Vehicle contact with surface irregularities such as potholes may induce significant vertical oscillations that can compromise the suspension system and diminish driving safety. Accelerometers can accurately detect high-acceleration spikes caused by potholes, facilitating surface condition categorization and evaluation [17].

The dynamics of land vehicles are intricately linked to surface quality and roughness [18,19]. Numerous methodologies and instruments exist for modeling this interaction; however, research using accelerometers and deep learning approaches, particularly neural networks, has provided advanced solutions for the more precise evaluation of surface impacts on vehicle dynamics [20,21]. The utilization of neural networks for evaluating surface conditions in the transportation sector enhances driving comfort and vehicle safety through the application of precise physical parameter data and advanced deep learning models [22].

These studies indicate that future research should involve in-depth examination of numerical methods and real-time surface classification algorithms, specifically targeting the classification of intricate and unpredictable surfaces such as pits or bumps [23].

Contemporary studies indicate that incorporating accelerometers and other sensors into automobiles facilitates the precise documentation of road surface vibrations and vehicle dynamics. A novel measuring device comprising a laser Doppler vibrometer (LDV) and an accelerometer, intended to assess the track conditions of a moving train, effectively estimated wheel–rail interaction forces via a dynamic vibration model [24]. This indicates that vibration monitoring using accelerometers is beneficial not just for road vehicles but also for railways [25] and other vehicular systems in assessing the health of structural components.

This study examined the use of several sensors, including accelerometers, and emphasized the issue that existing techniques like LiDAR and manual monitoring are costly and labor-intensive. Previous research indicates that accelerometers may provide an alternate method for vibration evaluation on different road surfaces; however, the measurement frequency of these sensors significantly affects the accuracy of the findings [26].

This study investigates the integration of GNSS and MEMS accelerometers for vibration monitoring in miniature systems. The integration of these sensors with software yields precise measurements of dynamic displacements. GNSS sensors provide exceptional sensitivity, rivalling high-end receivers, but MEMS accelerometers offer enough precision for high-speed vibration monitoring [27]. Previous research has indicated that sensor

amalgamation decreases the amplitude error by around 15%, yielding an average error of under 0.4 mm. This indicates that inexpensive GNSS sensors and accelerometers may serve as dependable sources for the precise measurement of dynamic displacements in automobiles and other structures.

Concurrent experiments have indicated that novel capacitive accelerometers, which enhance resonance frequency, achieve a measurement accuracy of 99.89% while decreasing power consumption to 0.11%. The research suggests novel techniques to minimize measurement errors via the optimization of the damping factor, allowing for very precise vibration measurements [28].

Accelerometer data are quite beneficial for assessing structural health. By incorporating millimeter-wave radars, accelerometers, and computational modules, the engineered systems can perpetually assess tiny and medium-sized buildings. These devices may provide long-term monitoring of structural dislocations, with measurements exhibiting an error margin of less than 0.1 mm [29]. This indicates that accelerometers are applicable not only in automobiles but also in architectural constructions to guarantee their stability and safety.

These studies demonstrate that vibration monitoring of minor buildings and the interpretation of accelerometer data are pertinent in both the transportation and construction industries. Vibration monitoring is a crucial aspect of component failure investigation. Fault analysis in hybrid integrated circuits indicates that accelerometer sensors enhance fault diagnostic accuracy using electrical parameter extraction and logic analysis methodologies to detect system malfunctions [30].

A significant study demonstrated the use of an artificial intelligence model created via the integration of Continuous Wavelet Transform (CWT) and Convolutional Neural Networks (CNNs) for the classification of road and load surfaces [31]. The research used acoustic sensors affixed to the vehicle to quantify TPIN (tire–pavement interaction noise) signals over seven distinct roadways. The model achieved 98.29% accuracy in categorizing seven road surfaces and 95.67% in categorizing 13 pavement types utilizing the data from these signals. The research demonstrated that the integration of auditory sensors with AI provides a dependable method for the real-time categorization of road surfaces while driving, particularly when well-chosen CWT filter sets and ideal data sequences are used.

The use of AI in evaluating road roughness is a significant subject, particularly for the prediction of surface irregularities. Separate analyzed research examined the forecasting of road surface roughness using artificial intelligence and emphasized the difficulties posed by insufficient data and human interpretation. The research advocated for concentrating on extensive datasets, including the historical IRI (International Roughness Index) and road maintenance and climatic data, to enhance model optimization and prediction precision [32]. The development of hybrid prediction models is a crucial element that may establish the primary focus of AI applications in road surface forecasting.

Liang et al. presented a real-time method for identifying road unevenness using serial acceleration signals and unevenness-correlated adaptive suspension damping control. The method uses a Long Short-Term Memory network to classify time domain signals into different unevenness classes. The algorithm's accuracy and robustness were demonstrated in a ground experiment, and the method's effectiveness was demonstrated through a calibration experiment [33].

Bystrov et al. emphasized the use of ultrasonic data for the categorization of road surfaces through statistical approaches in actual driving situations [34]. This indicates that ultrasonic signals may serve as a dependable method for evaluating road surface conditions. Environmental elements and vehicular motion might induce mistakes; hence, the study proposed methods to mitigate their impact, enhancing the precision of road surface categorization.

Zhao et al. created a large-scale road surface image dataset with detailed annotations for vehicle trajectory planning and active control systems. A convolutional neural network (CNN) classification model was trained, and a decision-level fusion method was proposed.

The models were deployed on an embedded hardware platform, achieving top-1 accuracy of 92.05% for the CNN and 97.50% after fusion [35].

Integrated sensor technologies, including acoustic and ultrasonic sensors, provide significant promise for the continuous monitoring of vehicle and road conditions. Acoustic sensors can identify sound waves produced by the vehicle's contact with the road surface, whilst ultrasonic sensors can sense vibrations resulting from the vehicle's tires engaging with road imperfections. These devices enhance real-time road condition monitoring while diminishing the need for expensive and labor-intensive human inspections.

The analyzed research indicates that artificial intelligence models, particularly those using hybrid methodologies like neural networks, have the potential to provide a standard solution for road surface categorization and prediction systems. Nonetheless, other problems pertain to the implementation of AI, particularly with the issues of data volume and integrity. Research indicates that current AI models often have data deficiencies, necessitating the creation of more extensive and inclusive datasets that include historical information, such as IRI and climatic conditions [36].

This paper's distinctiveness is attributed to its novel methodology for pavement categorization, using artificial intelligence (AI) approaches with data acquired from tire–pavement interaction noise (TPIN) sensors. This work is distinctive since it uses acoustic data for classifying road surfaces, in contrast to prior research that mostly utilized vibrations and mechanical sensors, including acceleration and displacement sensors. Furthermore, it employs Continuous Wavelet Transform (CWT) filters in conjunction with Convolutional Neural Network (CNN) architecture, facilitating the extraction of more precise information from temporal acoustic data.

The results of this endeavor aim to create and validate an accelerometer-based system for the real-time categorization of various road surface types using neural networks and logistic regression models. The objective is to assess the impact of various surfaces on the vehicle's vertical acceleration and stability, hence enhancing driving comfort and safety.

This article emphasizes real-time categorization via the integration of acoustic analysis and machine learning models, in contrast to previous studies that mostly use mechanical vibration models or geometry approaches for assessing road surfaces.

This method is characterized by its practicality; acoustic sensors may be mounted directly within the vehicle, enabling the continuous monitoring of road conditions throughout transit. This technique may be readily modified for commercial trucks, hence diminishing the need for more intricate and costly technology like LiDAR or other optical and laser sensors often used to evaluate road conditions.

2. Materials and Methods

Research experiments were conducted to quantify the unsprung mass during acceleration. A passenger automobile was used for experimental investigations. The car's weight during testing was 1350 kg, with overall dimensions of 4430 mm in length, 1814 mm in width, 1510 mm in height, and a wheelbase of 2685 mm. The tire size was 205/55 R16. To measure vehicle dynamics factors, the following sensors were installed on the vehicle.

Eight acceleration sensors were used, namely Analogue Devices ADXL327, with four designated for the wheels and four for sprung masses in the vertical axis. The dSpace Autobox device was used for data collection. The collected data were processed with Matlab R2022a software. The equipment used in the experiments is presented in Figure 1.

To precisely delineate the many surfaces used in the experiment, it was essential to provide a comprehensive study of each surface's physical attributes, its impact on vehicle dynamics, and its possible effect on the experimental outcomes. Each surface in this research had distinct characteristics that influenced the unsprung mass and vehicle acceleration data, which were essential for constructing a classifier based on accelerometer measurements.

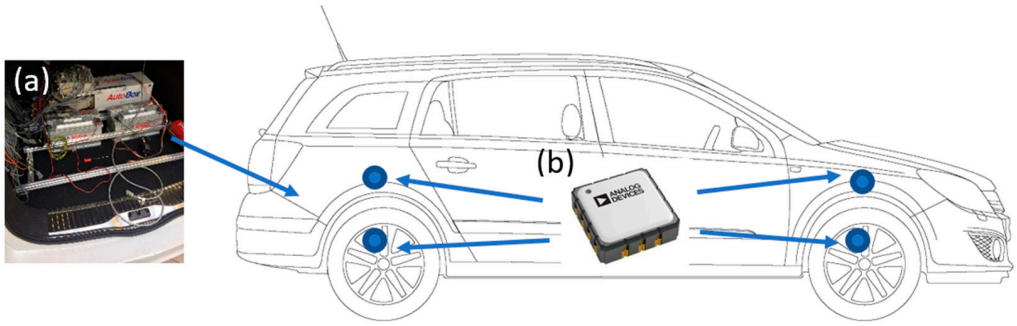

Figure 1. The experimental equipment installed in the vehicle: (**a**) Data collection machine dSpace Autobox with a DS2211 HIL 1/0 board and batteries; (**b**) accelerometer analogue devices ADXL327.

The "grater" surface denotes one of the most abrasive surfaces used in the experiment. It is distinguished by its irregular, gritty texture that resembles a grater, which is the origin of its name. This surface is often used on roadways as a provisional layer or in regions with severe weather when smooth asphalt is not a sustainable long-term option.

The coarse, irregular grater surface generates considerable vibrations in the car, particularly in the unsprung mass (wheels and suspension components), as the tires incessantly adapt to the little irregularities. The accelerometers affixed to the wheels captured high-frequency, substantial acceleration spikes in contrast to smoother surfaces. Consequently, the greater surface provided unusual accelerometer readings owing to its prominent roughness, rendering it a unique instance for surface categorization.

The "thump" surface, in contrast to the grater, denotes a rough surface characterized by fewer, more widely spread protrusions or elevations. These bumps are substantial and induce significant vehicle oscillations, however they occur less often than the greater surface irregularities.

This sort of surface is sometimes seen on inadequately maintained regional highways or locations where the surface is not routinely leveled. In this experiment, such a surface induced sporadic but significant vibrations when the vehicle's wheels encountered bigger bumps, followed by less intense vibrations in the intervals. The accelerometers recorded abrupt acceleration peaks as the vehicle travserved these bumps, yielding smoother readings in between, thereby creating a discernible pattern for categorization.

This surface indicates the existence of potholes, a prevalent problem on roadways, particularly in areas experiencing severe weather that leads to asphalt degradation. Traversing potholes exerted considerable strain on both the unsprung and sprung masses of a vehicle. The dimensions, depth, and configuration of potholes vary significantly, rendering their effect on vehicle dynamics uncertain.

When the vehicle's wheels encountered a pothole, the accelerometers registered abrupt, high-magnitude increases in acceleration. This presents a perilous scenario for the car, since substantial potholes may inflict damage at elevated speeds. Incorporating potholes into the experiment enabled the accelerometers to record anomalous data relative to other surfaces, owing to the abrupt and profound motions encountered by the wheels.

The concrete cube surface is a prominent urban pavement, particularly in the historic sections of European towns where it is often seen on streets. Concrete cubes possess a reasonably smooth surface; yet, the connections between the individual cubes induce minor, regular vibrations. This surface is resilient and enduring; yet, the joints may generate a faint rolling noise and persistent vibrations due to the vehicle's unsprung mass.

Accelerometers affixed to the vehicle's wheels documented little but constant acceleration spikes when the vehicle transversed the joints between the concrete blocks. Although less severe than the grater or thump surfaces, this pavement generated a consistent, low-intensity vibration pattern, manifesting in the accelerometer data as regular, slight oscillations.

Like the concrete cube, the surface of the basalt cube is composed of tiny individual stone pieces; however, the material used is basalt, a natural stone that has more strength and hardness than concrete. Basalt cubes have more durability than concrete; however, they possess comparable joint spacing that generates consistent vibrations when vehicles traverse them.

The impact of a basalt surface on vehicle dynamics would be similar to that of concrete cubes; however, the irregular texture of the natural stone may result in tiny variations in vibrations. The hardness and roughness of basalt may provide varying friction and vibration properties that the accelerometers would detect, resulting in a unique signature relative to concrete surfaces.

Cobblestone surfaces often consist of bigger stones in comparison to concrete or basalt cubes. This sort of surface is often seen in ancient metropolitan locales, especially in Europe, where cobblestones are used on roadways or walkways. Cobblestone surfaces are uneven and irregular, resulting in more noticeable gaps and inconsistencies among the stones.

Traversing cobblestones produced considerable and consistent vibrations in the vehicle's unsprung mass. The stones are often denser and bigger than concrete or basalt cubes, resulting in the accelerometers registering more substantial and frequent peaks in acceleration. Cobblestones provide a notably uneven surface that generates distinct vibrations, making it essential for classifier development.

Belgian cobblestone, like traditional cobblestone, consists of stone blocks; however, they are often placed in a more compact and systematic fashion, hence minimizing the imperfections between stones relative to normal cobblestone surfaces. Belgian cobblestones are renowned for their resilience and are often found in historic areas where roads and pathways have been maintained.

Traversing Belgian cobblestones induced significant vibrations in the unsprung mass, as the vehicle's wheels repeatedly contacted the interstices between the stones. The accelerometer data from this surface exhibited frequent, substantial oscillations like those generated by standard cobblestone, but with some variance attributable to the more structured arrangement of the stones. This made it one of the most abrasive surfaces in the experiment, imparting a distinctive vibration pattern to the classifier's training data.

The surfaces used in the experiment significantly affected the vehicle's dynamics, especially the unsprung mass, and uniquely modified the accelerometer measurements. Various surfaces, ranging from coarse textures such as graters and Belgian cobblestones to smoother materials like concrete and basalt cubes, generated unique vibration patterns that could be identified and categorized by accelerometer data. The differing degrees of roughness, stone dimensions, and joint intervals provided the necessary variability to train a classifier adept at differentiating between various road surfaces based on the patterns seen in the sensor data.

By comprehending the impact of various surfaces on vehicle dynamics, researchers may create a more precise categorization system, beneficial for applications like autonomous vehicle systems or road condition monitoring.

2.1. Neural Network

Neural network and multinomial logistic regression were used to recognize the pavement type. $D = \{(x_i, c_i) : 1 \leq i \leq n, x_i \in \mathbb{R}^m, c_i \in S\}$, where $S = \{s_1, s_2, \ldots, s_p\}$ denotes the set of pavement types. The sequence $x_i \in \mathbb{R}^m$ is a signal recorded from the accelerometer.

All measured parameters were captured at a frequency of 200 Hz using the dSpace Autobox system and subsequently analyzed on a computer using Matlab R2022a software. The main automotive I/O card was the DS2211 HIL 1/0 board. This allowed for the quick measurement of the required signals.

The vehicle was operated at a nearly constant speed of 30 km/h throughout testing. To provide precise statistics, the vehicle was driven many times on the aforementioned road surface.

To solve the classification problem, we applied the one-hot encoder $h : S \to \{0,1\}^p$ to the output variable as follows:

$$h(c_i) = \{y_{ij}\}_{1 \le j \le p}, \tag{1}$$

and

$$y_{ij} = \begin{cases} 0, & c_i \neq s_j, \\ 1, & c_i = s_j. \end{cases} \tag{2}$$

Below, we extracted dependences between the signal obtained from accelerometer and the pavement type by analyzing the data set $D = \{(x_i, y_i) : 1 \le i \le n, x_i \in \mathbb{R}^m, y_i \in \{0,1\}^p\}$. $(\Omega, \mathcal{F}, P)$ is the probability space and $Y : \Omega \to \{1, 2, \ldots, p\}$ is a random variable denoted by the type of pavement. The classification problem consists of the probability estimation $P(Y = j|x)$ that the pavement has type j based on recordered signal $x \in \mathbb{R}^m$ for $j \in \{1, 2, \ldots, p\}$.

Neural network is one of the most used types of machine learning and is usually utilized for classification or regression analysis [37–39]. A neural network structure consists of inputs, weights (parameters), aggregation functions, activation functions, and outputs. In multilayer networks, the inputs of the first layer are the predictors from the training set. In neural networks, the aggregation function is defined as the linear combination of the inputs and weights, and the result of the aggregation function is sent to the activation function g_j, defined as follows:

$$Z_j(x) = g_j(w_j Z_{j-1}(x) + \alpha_j), \tag{3}$$

where w_j denotes the weights, α_j for $j = 1, 2, ..., K$ is the bias, and for input layer, $Z_0(x) = x$. Thus, for neural networks containing K—layers, the inputs of the next layer consist from neuron, which are the values of activation function of the current layer. From (3) the last layer is defined as follows:

$$\begin{aligned} Z_K(x) = g_K(w_K g_K(w_{K-1} Z_{K-2}(x) + \alpha_{K-1}) + \alpha_K) = \ldots \\ = g_K(w_k g_{K-1}(w_{K-1} g_{K-2}(\ldots g_2(w_2 g_1(w_1 x + \alpha_1) + \alpha_2) \ldots) + \alpha_{K-1}) + \alpha_K) \end{aligned} \tag{4}$$

The three-layer neural network was utilized to analyze the road type. First, the road type as factor variable was coded (the category encoder was used).

For the first layer, the softsign activation function

$$softsign(x) = \frac{z}{|z|+1}, \tag{5}$$

was applied; for the second layer, the *relu* activation function

$$relu(z) = max\{0, z\}, \tag{6}$$

was used. For the last (output) layer, the *softmax* activation function

$$softmax(z) = \frac{1}{\sum_{j=1}^{k} e^{z_j}} (e^{z_1}, e^{z_2}, \ldots, e^{z_p}), \tag{7}$$

was applied; $1 \le i \le k$ and k denotes the numbers of categories of the output variable. To optimize the classification model, we used the cross-entropy as the cost function. Thus, for the classification problem based on neural network, the task consisted of solving the following problem:

$$minH(\{w_j\}_{1 \le j \le K}, \{\alpha_j\}_{1 \le j \le K}), \tag{8}$$

where the objective function was chosen as the cross-entropy as follows:

$$H(\{w_j\}_{1\leq j\leq K}, \{\alpha_j\}_{1\leq j\leq K}) = -\frac{1}{n}\sum_{i=1}^{n}\langle y_i, logZ_K(x_i)\rangle, \tag{9}$$

and $\langle\cdot,\cdot\rangle$ denotes the inner product of the output coded variable y_i and the output layer $Z_k(x_i)$, calculated as (3). The solution of the problem (8) needs to apply the backward propagation algorithm. Vector $softmax(Z_k(x))$ determines the probability distribution belonging to the class based on input variable $x \in \mathbb{R}^m$.

2.2. Multinomial Logistic Regression

Logistic regression [37,40–42] is a statistical model that describes the linear dependence of log odds on independent variables.

Multinomial logistic regression [37,43] describes the probability distribution of a random variable Y with respect to the input variable $x \in \mathbb{R}^m$. The probability that the observation $x \in \mathbb{R}^m$ comes from j-th class:

$$P(Y = j|x) = \frac{e^{\langle(1,x),\beta_j\rangle}}{\sum_{k=1}^{p} e^{\langle(1,x),\beta_p\rangle}}, \tag{10}$$

where $\beta_j = (\beta_{0j}, \beta_{1j}, \beta_{2j}, ..., \beta_{mj})$ denotes the parameters of logistic regression for j-th class, $j \in 1, 2, \ldots, p$.

When the random variable Y is encoded as a one-hot-encoding vector, i.e., the j-th class corresponds the vector $y = (y_1, y_2, \ldots, y_p)$, where $y_j = 1$ and $y_i = 0$ for $i \neq j$, $1 \leq i \leq p$), then the probability is as follows:

$$P(Y) = y|x) = \prod_{j=1}^{p}\left(\frac{e^{\langle(1,x),\beta_j\rangle}}{\sum_{k=1}^{p} e^{\langle(1,x),\beta_p\rangle}}\right)^{y_j} = \frac{\prod_{j=1}^{p}\left(e^{\langle(1,x),\beta_j\rangle}\right)^{y_j}}{\sum_{k=1}^{p} e^{\langle(1,x),\beta_p\rangle}}. \tag{11}$$

We assume that the observations are drawn randomly. For data set $D = \{(x_i, y_i) : 1 \leq i \leq n, x_i \in \mathbb{R}^m, y_i \in \{0,1\}^p\}$, we define the likelihood function $L(\beta)$ as follows:

$$L(\beta) = \prod_{i=1}^{n} P(Y = y_i|x_i) = \prod_{i=1}^{n}\prod_{j=1}^{p}\left(\frac{e^{\langle(1,x_i),\beta_j\rangle}}{\sum_{k=1}^{p} e^{\langle(1,x_i),\beta_p\rangle}}\right)^{y_{ij}}, \tag{12}$$

where $\beta = (\beta_1, \beta_2, \ldots, \beta_p)$. The identification of multinomial logistic regression consists of the solution the following task:

$$\max_{\beta} \quad L(\beta), \tag{13}$$

Instead of solving task (13) we solved the auxiliary task:

$$\max_{\beta} \quad lnL(\beta), \tag{14}$$

we estimated β_j the unknown parameters of multinomial logistic regression, where from (11) and (12), the logarithm of likelihood function is given by the following formula:

$$lnL(\beta) = \sum_{i=1}^{n}\left(\sum_{j=1}^{p} y_{ij}\langle(1,x_i),\beta\rangle - ln\left(\sum_{k=1}^{p} e^{\langle(1,x),\beta_p\rangle}\right)\right). \tag{15}$$

When the predictors are correlated, we used regularization [44,45] to receive better predictions. In the presented case, ELASTICNET was also used. The parameters of multinomial logistic regression are determined by solving the following task:

$$\max_{\beta} \sum_{i=1}^{n} \left(\sum_{j=1}^{p} y_{ij} \langle (1, x_i), \beta \rangle - ln \left(\sum_{k=1}^{p} e^{\langle (1,x), \beta_p \rangle} \right) \right) - \lambda P_\alpha(\beta), \tag{16}$$

where $\lambda > 0$, $0 \leq \alpha \leq 1$ and P_α denotes the penalty calculated as follows:

$$P_\alpha(\beta) = \alpha \| \beta \|_{L_1} + \frac{1-\alpha}{2} \| \beta \|_{L_2} = \sum_{j=1}^{p} \left(\alpha |\beta_j| + \frac{1-\alpha}{2} \beta_j^2 \right). \tag{17}$$

After estimating the parameters of multinomial logistic regression, we determined the probabilities of membership to each class by using Formula (11).

2.3. Accuracy Matrices

The basic terminology and coefficients describing the quality of the classifier are presented below [37,46]. For each class, we defined a confusion matrix. For the j-th class, we defined the membership of this class as a positive case and we took the membership of the other classes as a negative case.

The confusion matrix presented in Table 1 contains the following values:

Table 1. Confusion matrix for classifier performance evaluation.

	Predicted Positive	**Predicted Negative**
Positive	TP	FN
Negative	FP	TN

TP (True Positive) denotes the number of cases for which membership of the j-th class is correctly identified,

TN (True Negative)—the number of cases for which membership of other classes was correctly recognized,

FP (False Positive)—the number of cases for which a signal belonging to other classes was recognized as a signal of the j-th class,

FN (False Negative)—the number of cases for which a signal originating from class j-th was recognized as a signal belonging to the other classes.

Below, we use the following basic characteristics to describe the quality of the classifier:

Accuracy denotes the part of samples which were correctly identified:

$$Accuracy = \frac{TP + TN}{TP + TN + FP + FN}. \tag{18}$$

The true positive rate is the proportion of cases belonging to the j-th class that are correctly recognized by the model:

$$True\ Positive\ Rate(TPR) = Sensitivity = \frac{TP}{TP + FN}. \tag{19}$$

Specificity is the proportion of cases not belonging to the j-th class that are correctly classified by the model:

$$Specificity = 1 - False\ Positive\ Rate(FPR) = \frac{TN}{TN + FP}. \tag{20}$$

The Positive Predicted Value is the proportion of cases belonging to the j-th class among those predicted by the model as belonging to the j-th class:

$$Positive\ Predicted\ Value(PPV) = Precision = \frac{TP}{TP + FP}\ , \tag{21}$$

The Negative Predicted Value is the proportion of cases not belonging to the j-th class among those predicted by the model as not belonging to the j-th class:

$$Negative\ Predicted\ Value(NPV) = \frac{TN}{TN + FN}\ , \tag{22}$$

Prevalence is the proportion of samples belonging to the j-th class:

$$Prevalence = \frac{TP + FN}{TP + TN + FP + FN}\ , \tag{23}$$

The Detection rate is the proportion of samples that are correctly classified by the model as belonging to the j-th class:

$$Detection\ Rate = \frac{TP}{TP + TN + FP + FN}, \tag{24}$$

Detection prevalence is the proportion of samples that are classified by the model as belonging to the j-th class:

$$Detection\ Prevalence = \frac{TP + FP}{TP + TN + FP + FN} \tag{25}$$

Balanced accuracy is a mean between sensitivity and specificity:

$$Balanced\ Accuracy = \frac{Sensitivity + Specificity}{2} \tag{26}$$

The False Alarm Rate is the proportion of cases misclassified by the model as belonging to the j-th class:

$$False\ Alarm\ Rate = \frac{FP}{TP + FP} \tag{27}$$

Additionally, a Receiver Operating Characteristic (ROC) curve and Area Under the Curve (AUC) was determined for each class.

For this purpose, using the function $softmax$ for neural networks and using Formula (10) for multinomial logistic regression, we determine the membership probabilities for each class. For the j-th class ($j \in \{1, 2, \ldots, p\}$) for different cut-off levels (thresholds) $0 \leq c \leq 1$ we determine a confusion matrix, where we score the i-th case as positively recognized if $P(Y = j|x_i) \geq c$ otherwise as negatively recognized for $1 \leq i \leq n$. Based on the confusion matrix, we determine the FPR ($1 -$ Specificity) and the TPR and place the points in the coordinate system.

For different thresholds, we determine the confusion matrices and calculate the fraction of positive outcomes of the total positives and the fraction of false positives of the total negatives. Thus, the sensitivity and specificity depend on the selected threshold (cut-off value). In the coordinate system FPR–TPR, we mark the points that correspond to the selected threshold and create ROC curves which is a graphical presentation of classifier performance, as the threshold (cut-off level) is varied. For a higher cut-off value, the false positive rate will decrease (specificity will increase) and the true positive rate (sensitivity) will also decrease. For a lower cut-off value, the true positive rate and the false positive rate will increase. The behavior of the classifier across different thresholds is calculated as the area covered below the ROC curve and is called the Area Under the Curve (AUC) [47,48].

Larger AUC values correspond to better recognition by the classifier. For AUC = 1, we have a perfect classifier.

3. Results

The impact of various pavement types on vehicle vertical acceleration was examined, emphasizing their effect on vehicle dynamics, especially unsprung mass. Accelerometer data were used to examine several surfaces, each generating distinct acceleration patterns influenced by their unique physical features, which impact the vehicle's comfort, stability, and mechanical integrity. The experiment's findings demonstrate how varying textures and imperfections of surfaces result in distinct vertical strains inside the vehicle suspension, offering significant insights regarding pavement categorization.

Figure 1 illustrates the acceleration of the vertically suspended mass as measured by the accelerometer while the vehicle traversed a grate-type surface. The characteristics of this surface induce very intense and frequent vibrations, as seen by the graph displaying acceleration peaks fluctuating between +150 m/s^2 and −100 m/s^2. This surface produces quick oscillations that significantly influence the vehicle's dynamics, particularly its unsprung mass (wheels and suspension), owing to the pronounced and regularly varying irregularities. Initially, Figure 1 shows an acceleration around zero (up to about 0.2 s), suggesting that the vehicle is either commencing movement or traversing a far smoother surface prior to reaching the grating. At 0.3 s, pronounced and frequent changes in acceleration are evident, plainly indicating surface irregularities. The most significant accelerations reach +150 m/s^2, indicating substantial vertical pressures exerted on the vehicle's sprung mass.

This coating substantially influences the vehicle's comfort and stability. Figure 1 indicates that the driver would have significant pain due to the extreme vertical acceleration, while the car's suspension would be perpetually exposed to substantial stresses. Such variations may lead to accelerated deterioration of suspension systems and wheels, as well as impacting driving safety.

Figure 2 indicates that after 0.9 s of acceleration, the peaks diminish and stabilize, suggesting that the vehicle has transitioned from a "grating" surface to a smoother terrain or has decelerated. Consequently, the "Grater" surface induces abrupt and intense oscillations, which are clearly evident in the graph, and these findings suggest that this coating is among the most irregular used in the experimental analysis.

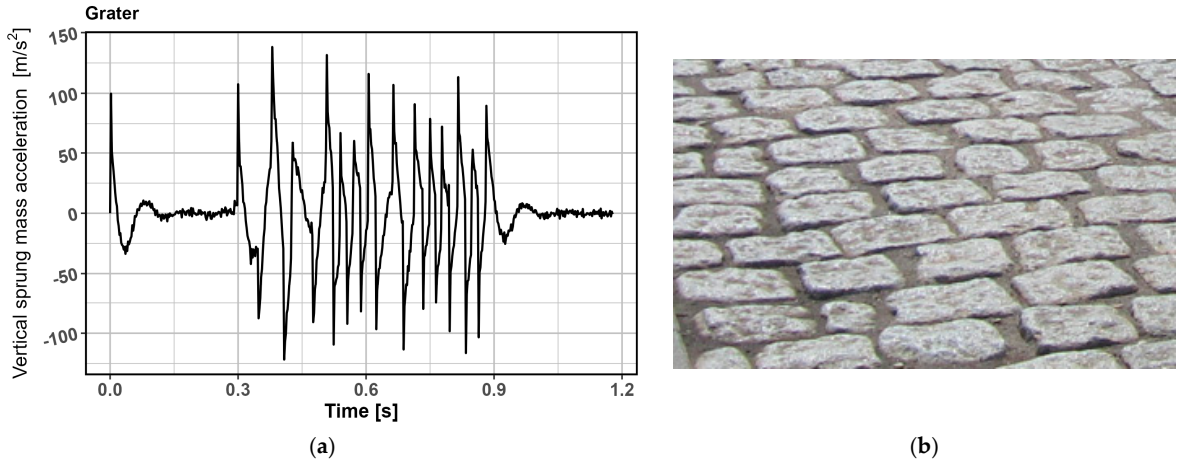

Figure 2. The acceleration profile of vertically sprung mass on a grater-type surface: (**a**) the acceleration graph; (**b**) an example of the surface.

Figure 3 illustrates a "thump" surface, characterized by greater but less frequent irregularities. This surface type is marked by infrequent but significant changes in the vehicle's dynamic behavior. In contrast to a grater surface, where vibrations are consistent

and frequent, acceleration fluctuations here occur sporadically when the wheels traverse a succession of discrete bumps.

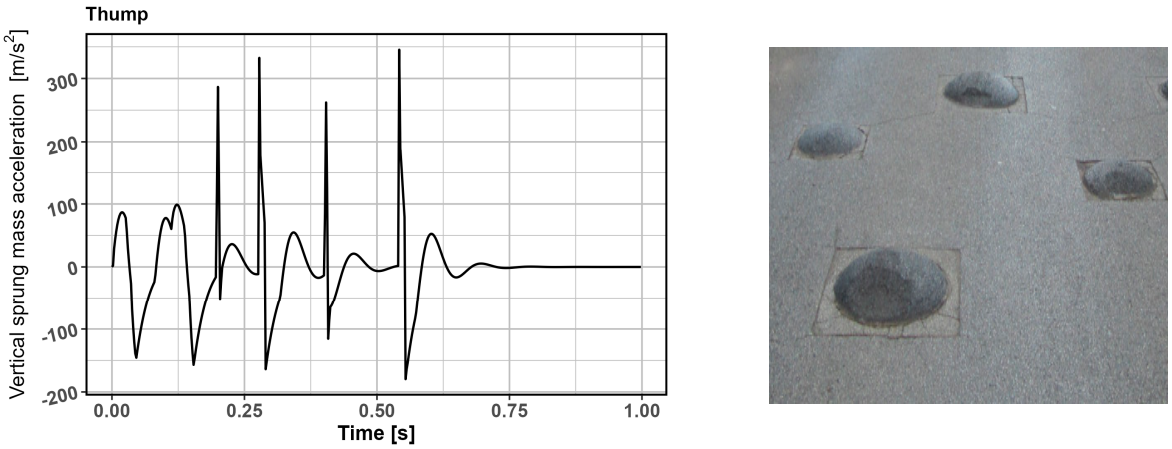

(**a**) (**b**)

Figure 3. The acceleration peaks observed on a thump surface with large irregularities: (**a**) the acceleration graph; (**b**) an example of the surface.

At the start of Figure 3 (0 s), minor, consistent oscillations are seen, perhaps indicative of the vehicle traversing minor irregularities or transitioning onto a surface characterized by abrupt "thump" bumps from a smooth terrain. Initial significant increases in acceleration transpire within around 0.1 s when the wheels contact a substantial bump, yielding an acceleration value of approximately +200 m/s^2.

Figure 3 illustrates a sequence of significant fluctuations, each characterized by distinct peaks as the acceleration varies dramatically. A secondary peak emerges at around 0.25 s, exhibiting acceleration values reaching +300 m/s^2, indicating a substantial or intensified perturbation on the surface to which the vehicle's sprung mass responds. Following each peak, the vertical acceleration rapidly declines, often reaching almost −100 m/s^2 or lower, indicating significant oscillations in the sprung mass as the wheels descend off the bump.

Following 0.5 s of acceleration, the jumps diminish, and by 1 s, the graph approaches a linear trajectory, suggesting that the vehicle has either decelerated or passed the largest obstacles and returned to a smoother surface.

The thump surface, while exhibiting less irregularities than the grate surface, substantially impacts the vehicle, particularly when the wheels strike singular huge protrusions. These leaps may induce abrupt variations in acceleration, as seen in the graph, and exert significant stress on the vehicle's suspension and unsprung mass. The accelerometer captures significant variations in acceleration whenever the wheels traverse a bump, enabling it to derive data specific to this surface type.

The primary issue presented by potholes (Figure 4) is the abrupt displacement of the unsprung mass (wheels and suspension) during the entry and escape of the wheels from the pothole. Figure 4 demonstrates the impact of abrupt changes on vehicle dynamics.

Beginning at 0 s, Figure 4 illustrates a rather smooth trajectory of vertical acceleration, with minor oscillations either attributable to typical surface imperfections or the transitional phase before the car encounters the potholes. Beginning at around 0.3 s, the acceleration exhibits notable fluctuations, suggesting that the wheels are beginning to meet minor irregularities in the road surface, such as tiny bumps or minor potholes; however, these variations are not yet as strong as those shown later in Figure 3.

A very strong acceleration peak, surpassing +200 m/s^2, is found between 0.9 and 1.1 s. This is a certain indication that the vehicle's wheels have encountered a substantial pothole. Concurrently, just after this apex, the acceleration declines to around −150 m/s^2, indicating that the car exited the pit shortly thereafter. Sudden increases in vertical acceleration are

characteristic of traversing deep potholes, as the wheels quickly plunge into the depression and then emerge, resulting in significant effects on the vehicle.

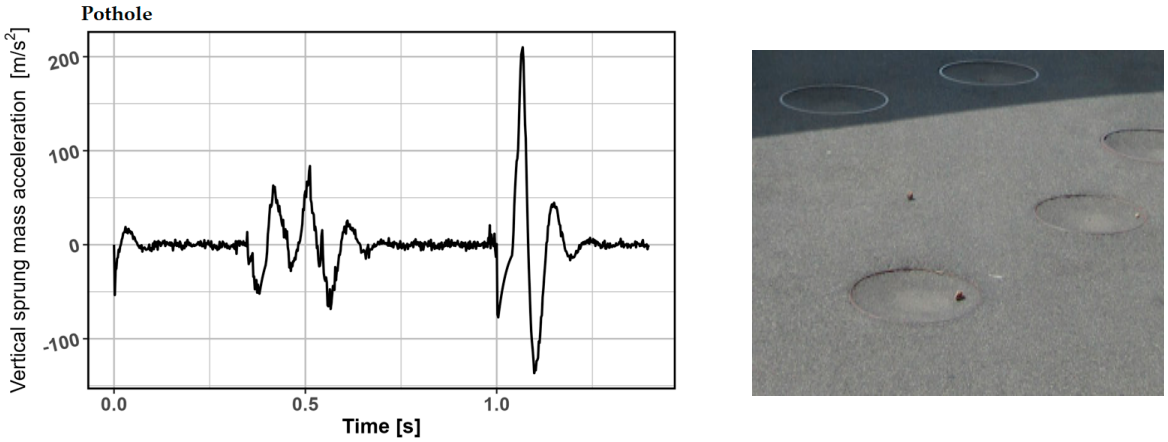

(**a**) (**b**)

Figure 4. The impact of potholes on vehicle vertical acceleration and dynamics: (**a**) the acceleration graph; (**b**) an example of the surface.

The significant fluctuation in acceleration during the one-second interval signifies the most substantial external influence on the sprung mass during the experiment. This impacts both the vehicle's suspension system and the quality and safety of driving. This coating may inflict significant harm on the vehicle's wheels and suspension, particularly at elevated speeds.

Subsequent to this disturbance, the acceleration normalizes, and within 1.2 s, the trajectory approaches linearity, indicating that the vehicle now traverses calmer terrain or minor irregularities after a significant pothole.

Figure 4 clearly illustrates that the effect of potholes on a vehicle is notably severe, since deep potholes induce significant vertical accelerations that fluctuate rapidly between high and low values. This substantially impacts the vehicle's stability, and potholes might be among the most hazardous surfaces, concerning both possible damage to the automobile and the driver's comfort.

Figure 5 illustrates the acceleration of a vertically suspended mass as it traverses a surface composed of concrete cubes. This pavement is often used in urban settings, particularly in historic sections of European towns where streets or pavements are covered with concrete tiles or cubes. This coating has uniform intervals between the cubes, resulting in constant although comparatively milder vibrations than those produced by coarser coatings like grates or pits.

Figure 5 clearly illustrates variations in acceleration at a rather regular frequency, indicative of the continuous interaction between the wheels and the interstices of the concrete cubes. Between 0 and 0.25 s, the graph illustrates an early, rather smooth motion with acceleration values marginally above ± 50 m/s^2. This may indicate that the vehicle gradually contacts the surface or starts to traverse the cubes, albeit the impact is not yet as pronounced.

Acceleration jumps become increasingly evident after 0.3 s, with several peaks exceeding ± 100 m/s^2, suggesting that the wheels are traversing gaps in tiles or cubes. Each apex in Figure 5 represents the contact of the wheels with the interstices between the tiles. These oscillations produce discernible although relatively weak vibrations that persist, owing to the uniform configuration of the concrete cubes. In contrast to traversing uneven terrains like potholes or ruts, this pavement type lacks significant, abrupt acceleration variations; yet, consistent vibrations do impact the vehicle's unsprung mass.

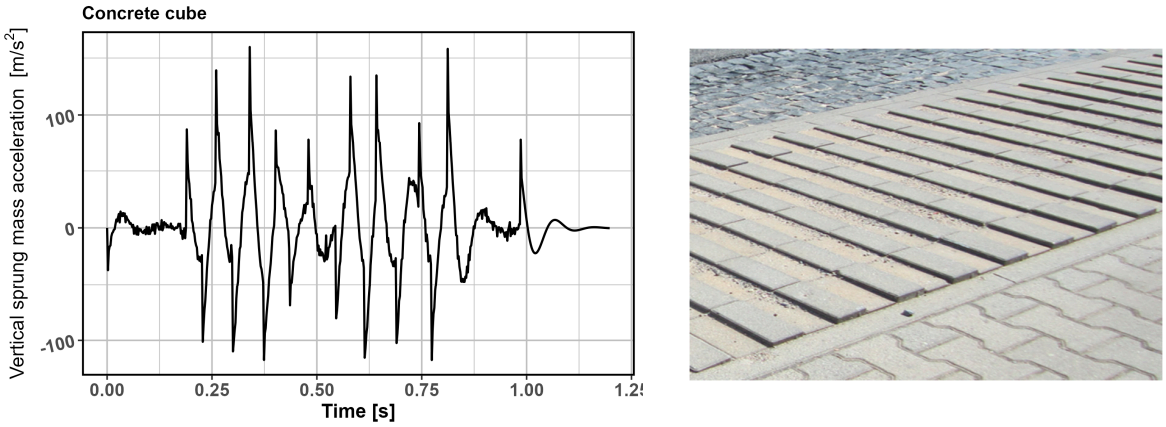

Figure 5. The acceleration variations on a concrete cube pavement with regular intervals: (**a**) the acceleration graph; (**b**) an example of the surface.

Beginning at around 0.75 s in Figure 5, there is a reduction in the peaks, and the variations in acceleration become less significant. This may suggest that the vehicle has decelerated or transitioned into a smoother area where the tile gaps are less perceptible. Ultimately, from the 1 s mark onwards, the line approaches linearity, signifying a reduction in vibrations and maybe signaling that the car has departed off the concrete cube pavement.

This surface, although not as coarse as a pit or grate, generates persistent, low-intensity vibrations that aggregate over an extended duration. The vehicle's suspension is perpetually exposed to stresses from the wheels traversing the gaps between the concrete cubes, perhaps resulting in a little but enduring loss of stability and discomfort for the occupants. The dynamics shown in Figure 5 indicate that each tile gap produces minor acceleration fluctuations; yet, owing to the uniform configuration of the tiles, the accelerometer captures rather stable data instead of erratic spikes typical of other surfaces. The coating of the concrete cubes, although producing reduced amplitude vibrations, provides a distinctly recognizable signal that can be detected by the accelerometer, owing to the consistent interstices between the cubes. This signal has a greater frequency and lower amplitude relative to rougher surfaces, although it still yields distinctive data beneficial for surface categorization algorithms.

Figure 6 illustrates the acceleration of a vertically suspended mass traversing a cobblestone surface. The pavement has an irregular structure, with stones varying in size and form, resulting in pronounced disparities in surface relief due to the spaces between them. These qualities result in the generation of frequent but uneven vibrations while traversing stones, as plainly seen in Figure 6.

Between 0 and 0.2 s in Figure 6, a very subdued acceleration pattern is seen, characterized by minor and consistent vertical variations, suggesting that the vehicle has not yet encountered a significant rocky terrain or is operating at low velocities. However, from 0.25 s onwards, there are clearly more significant oscillations, indicating that the car has passed over a rougher section of stone pavement. The acceleration measurements exhibit significant fluctuations of ± 100 m/s^2, indicating that the vehicle's wheels encounter unevenly placed stones.

The most significant increases in acceleration occur between 0.25 and 0.5 s, characterized by strong and irregular vertical acceleration, accompanied by a high frequency of leaps. The variation in stone pavement features may contribute to this phenomenon; in some areas, bigger stones induce more shocks to the vehicle's suspension, whilst in other regions, narrower gaps between stones result in milder but nevertheless frequent oscillations.

At the conclusion of Figure 6, at about 0.6 s, the increments in acceleration progressively diminish, and from 0.75 s onwards, the variations stabilize almost completely. This

may suggest that the vehicle has completed traversing the most arduous section of the roadway, or that the velocity has diminished, resulting in fewer oscillations.

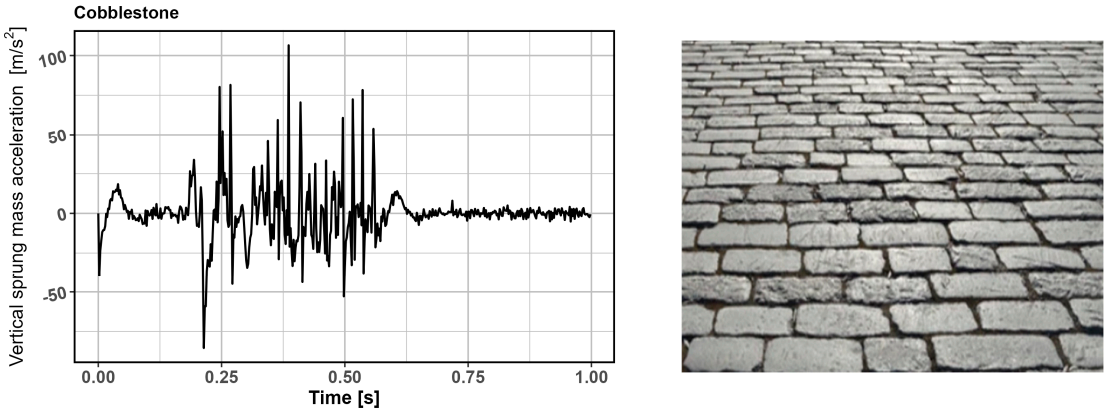

(**a**) (**b**)

Figure 6. The dynamic response of vertically sprung mass on a cobblestone pavement: (**a**) the acceleration graph; (**b**) an example of the surface.

Stone pavement generates consistent although sometimes unpredictable vibrations that particularly impact the unsprung mass. Each stone in the pavement generates varying intensities of shock based on its dimensions and placement. This indicates that the vehicle's wheels are perpetually subjected to varying shocks, necessitating a rapid response from the suspension to continuously fluctuating irregularities. Consequently, the level of driving comfort on such a surface is significantly diminished, and the frequent and pronounced acceleration fluctuations seen in Figure 6 illustrate this dynamic load.

The stone pavement induces persistent, moderate-intensity jolts to the vehicle, resulting in discernible although irregular acceleration spikes. The elevated oscillation frequency shown in Figure 6 signifies that this pavement produces substantial data for the accelerometers, and its irregular vibration patterns are crucial for the analysis and classification of pavement types based on the accelerometer data.

Figure 7 illustrates the acceleration of the vehicle's vertical sprung mass when traversing Belgian cobblestone. This pavement has an irregular surface composed of bigger, inconsistently spaced stones, often seen in historical urban thoroughfares or historic areas. In contrast to traditional stone pavements, Belgian paving has deeper interstices between the stones and more pronounced changes in surface texture, resulting in heightened and more powerful vibrations.

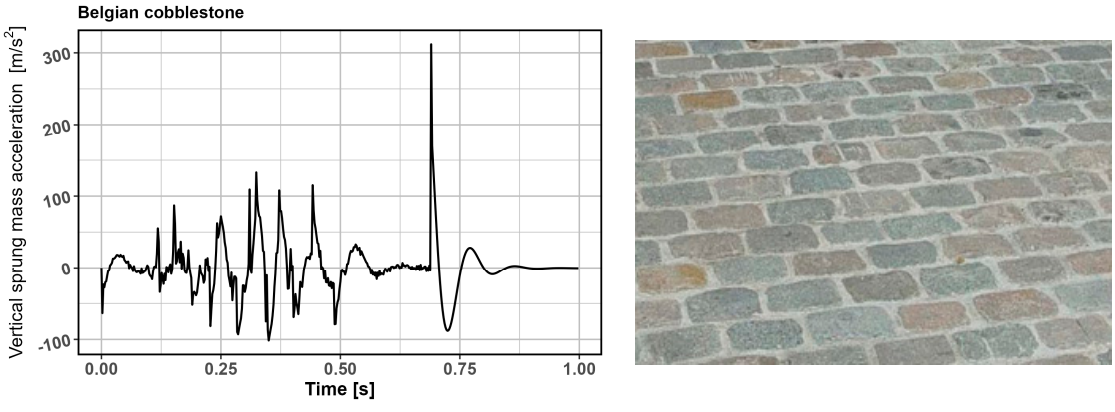

(**a**) (**b**)

Figure 7. Vertical acceleration analysis on a Belgian cobblestone surface: (**a**) the acceleration graph; (**b**) an example of the surface.

Initially, between 0 and 0.25 s, minor fluctuations in acceleration are seen, ranging from +50 m/s^2 to −50 m/s^2. This signifies that the vehicle is either approaching a section of stone pavement or traversing a less severe portion of this surface. Throughout this interval, the vibrations are comparatively less; yet, it is evident that the surface influences the vehicle's dynamics.

After 0.3 s of acceleration, the jumps become more prominent and frequent, oscillating between +150 m/s^2 and −100 m/s^2. This signifies that the vehicle is traversing a more rugged section of roadway where the wheels are continually striking bigger stones or deeper crevices between them. The vibrations intensify, increasing stress on the vehicle's unsprung mass and suspension system. This segment of the length reveals that the car endures consistent but irregular impacts.

Between 0.7 and 0.8 s, there is a pronounced rise in acceleration exceeding +300 m/s^2, subsequently followed by a swift decline to −100 m/s^2. This may suggest that the wheels have encountered a substantial rock or bump, resulting in a significant shock to the vehicle's suspension and its sprung mass. Such leaps may pose significant risks to a vehicle, since they impose substantial pressures on both the wheels and the chassis, with Figure 6 illustrating their abruptness and severity.

At 0.85 s, the acceleration changes begin to stabilize, and by 0.9 s, the line approaches linearity, signifying a reduction in vibrations or the conclusion of the vehicle's traversal over the stone pavement. This may indicate that the car moves onto a smoother terrain or decelerates, therefore reducing vibrations.

Belgian cobblestone pavement has huge stones with pronounced interstices, resulting in significant and irregular effects on the vehicle's unsprung mass. In contrast to smoother surfaces, such as concrete tiles or standard stone pavement, Belgian pavement produces significant and irregular acceleration spikes. The abrupt spike shown in the graph at the 0.75 s interval signifies that such a surface might produce hazardous forces while the vehicle is moving at elevated speeds.

Belgian stone pavers generate more powerful and robust vibrations than standard stone pavers owing to their bigger stones and deeper interstices. This produces significant and pronounced spikes in acceleration, as seen in the graph, and these data may be crucial for surface classification algorithms to identify this kind of pavement from accelerometer readings.

Basalt paving (Figure 8), similar to other stone pavements, produces an irregular surface owing to the configuration of the stones, their placement, and the interstices between them. Basalt is a natural, resilient stone often used in urban roadways due to its durability and resilience; yet, it produces a coarse and rigid surface that induces significant vibrations in vehicles.

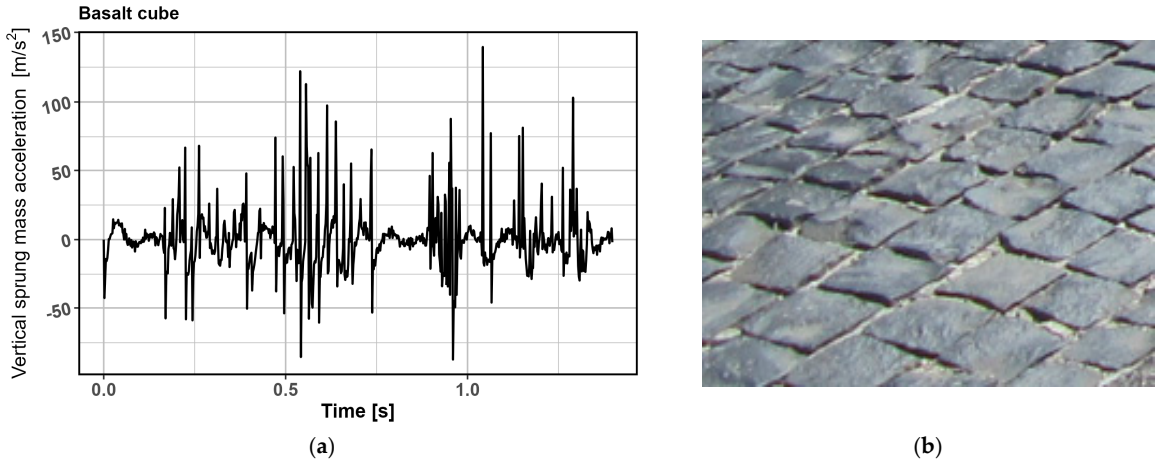

Figure 8. The vertical acceleration of the vehicle on a basalt cube pavement: (**a**) the acceleration graph; (**b**) an example of the surface.

Between 0 and 0.25 s, the acceleration curve exhibits minor oscillations with an amplitude of up to ± 50 m/s^2. This illustrates the car's first, relatively smooth traversal over the basalt pavement prior to the wheels encountering more pronounced imperfections. Despite the diminutive size of the gaps in the basalt pavement, these fundamental oscillations demonstrate that even little contact with the stones induces vibrations detectable via the accelerometer data.

Between 0.3 and 0.7 s, there are notable acceleration spikes ranging from +150 m/s^2 to -100 m/s^2. This signifies that the vehicle has traversed a more severe area characterized by bigger stones or more pronounced gaps between them. Basalt pavement is often coarse, resulting in increased vertical stresses on the vehicle as the wheels continuously adapt to the surface imperfections. Each stone, or the interstitial gap, generates immediate but substantial shocks detected by the accelerometer.

Near the conclusion of the graph, between 0.8 and 1.2 s, the acceleration spikes further, with some values above +150 m/s^2. These abrupt jolts may signify that the vehicle has encountered a notably irregular segment of basalt pavement or a more substantial void between the stones. These oscillations indicate abrupt and significant changes in the vehicle's sprung mass, which particularly impact driving comfort and the suspension system.

Basalt pavement generates consistent but irregular vibrations owing to the configuration and morphology of the natural stone. The stone's rigid roughness results in surface imperfections that enhance vertical acceleration and significantly impact the vehicle's suspension and unsprung mass. The accelerometer detects significant shocks when the wheels traverse bigger gaps or notably uneven stones, and these signals are prevalent, owing to the irregular pavement construction.

The hardness and irregular surface of basalt pavement provide considerable vibrations for the car. The graph clearly illustrates that the acceleration spikes produced by this pavement are irregular and pronounced, particularly when the wheels contact bigger stones or spaces between them. This pavement type generates frequent and intense vibrations that may be unique in the accelerometer signal dataset, which is crucial for surface classification methods to identify this pavement type from accelerometer data.

4. Discussion

For each type of pavement, such as grater, thump, pothole, concrete cube, basalt cube, cobblestone, or Belgian cobblestone, 100 signals recorded with the accelerometer were analyzed, i.e., for the i-th sample, the time series $\{v_{it}\}_{1 \le t \le h_i}$, $1 \le i \le 700$ was analysed. Each time series was ordered as $v_{(1)} \le v_{(2)} \le \ldots v_{(h_i)}$ and the quantiles of the order $0, d, 2d, \ldots, 1$ were estimated, where $d = 0.05$. For the i-th sample, the sequence $x_i = (v_{(1)}, v_{([dh_i])}, v_{([2dh_i])}, \ldots, v_{(h_i)})$ was determined. Thus, inputs of the dataset were defined as quantiles obtained from the raw signals, which can be treated as an approximation of the empirical cumulative distribution function for the readings obtained from the accelerometer.

For sequence $\{y_i\}_{1 \le i \le n}$, $y\_i \in$ {"*grater*, *thump*, *pothole*, *concrete cube*, *basalt cube*, *cobblestone*, *Belgian cobblestone*"} was applied for one-hot-encoding. Therefore, the data frame $D = \{(x_i, y_i) : 1 \le i \le n, x_i \in \mathbb{R}^{21}, y_i \in \{0,1\}^7\}$ was defined. Next the data set was split randomly into a learning set (containing 80% cases) and a test set (20% cases).

4.1. Neural Network Classifier

A 3-layer neural network was used to classify the pavement. Table 2 presents the structure of the neural network, but Figure 9 presents the scheme of data processing and learning process using a neural network for pavement identification.

Table 2 illustrates the outcomes of the deep neural network architecture, focusing on the configuration of the network layers and their impact on the final classification results. The output of the first dense layer, including 15 neurons with softsign activation, indicates that this layer effectively regulates substantial input levels. The softsign activation function normalizes values between -1 and 1, mitigating significant volatility and enhancing

the stability of the learning process. The softsign function was used to emphasize the differences resulting from the application of aggregation of the results obtained after quantile standardization. Consequently, the network enhances its ability to identify diverse data patterns, leading to more reliable and consistent outcomes.

Table 2. Confusion matrix for classifier performance evaluation.

Layer (type)	Output Shape	Parameters	Activation
Input Layer	(1, 21)	0	
Dense 1	(1, 15)	330	*softsign*
Dense 2	(1, 10)	160	*relu*
Output Dense	(1, 7)	77	*softmax*

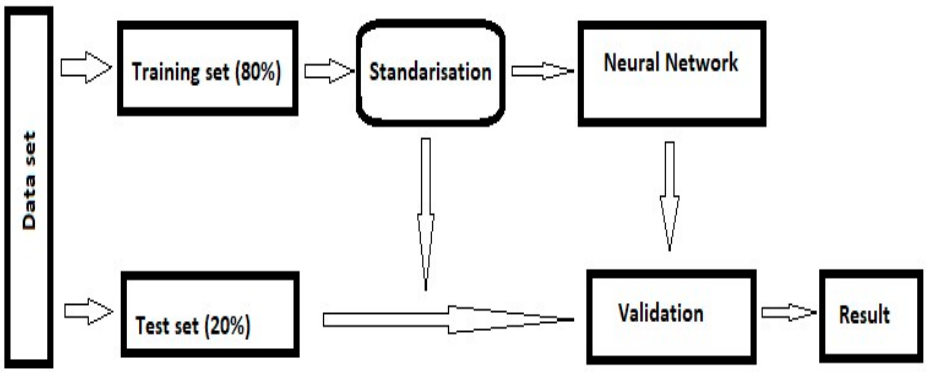

Figure 9. The data processing scheme and learning process using a neural network for pavement identification.

The second dense layer, including 10 neurons with ReLU activation, conveys significant insights into neuronal activity since ReLU eliminates negative values and permits only positive values to affect the output. This method is significant since it preserves network simplicity, decreases computing complexity, and enhances accuracy. The ReLU function enhances the network's learning velocity, facilitating expedited convergence.

The final output layer, using softmax activation, delivers the network's ultimate predictions: seven probabilities indicating the extent to which a data point is associated with a certain class. The probabilistic outcomes of this layer facilitate the interpretation of the model's performance and enable the assessment of the classifier's accuracy based on the network's recognition of each class. The network produces 567 parameters, enabling the model to execute intricate classification tasks while preserving an optimal balance between accuracy and processing efficiency.

The total number of parameters of the neural network is 567. The number of training epochs is 200. Validation was also applied during learning in each epoch. In each epoch, the batch was divided into a training set, containing 90% of the batch, and a validation set, containing 10% of the batch. Cross-entropy was selected as the quality function for the classification model based on the neural network, and the accuracy was chosen as a verification metric.

Figure 10 shows the cross-entropy and accuracy values during the neural network training. The cross-entropy graph illustrates the reduction in the loss function for both the training and validation datasets. Initially, the cross-entropy is high (about 2.0), indicating that the model starts learning with poor precision and misclassifies the data. Nonetheless, with the passage of time, particularly after the first 50 epochs, the entropy value markedly diminishes, and both curves consistently decline towards a near-zero value. This indicates that the model increasingly improves its efficiency in minimizing mistakes and refining categorization for both training and validation datasets. The cross-entropy stabilization

indicates that the model is not in significant danger of overfitting and effectively generalizes the findings.

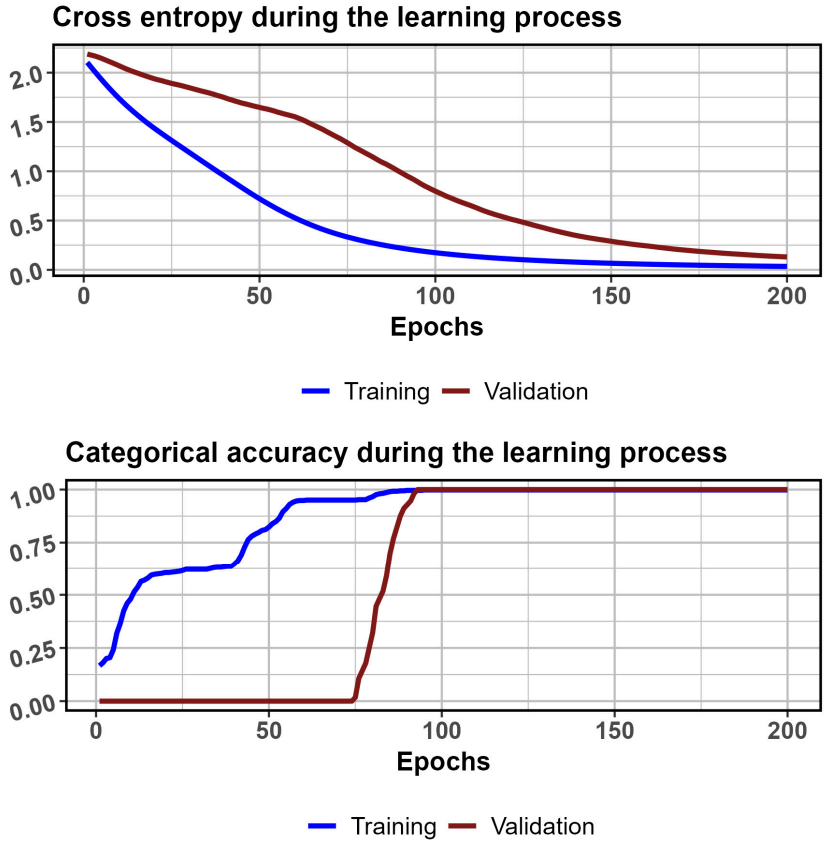

Figure 10. Cross-entropy and accuracy during the neural network learning process.

Figure 10 depicting category accuracy demonstrates an upward trend. Initially, the training accuracy escalates swiftly, reaching about 100% after around 50 epochs. Simultaneously, the validation accuracy first ascends at a gradual pace; nevertheless, after 75 epochs, it experiences a significant surge, ultimately approaching 100%.

This indicates that the model accurately classifies the training data throughout the learning phase and effectively generalizes it to the validation data, which is crucial for ensuring optimal performance with novel data. The reduction in cross-entropy and the improvement in categorical accuracy demonstrate that the model has successfully acquired the ability to categorize the data, maintaining consistent performance within both the training and validation datasets. This indicates that the model is well calibrated since there are no apparent indications of overfitting or inability to handle fresh data.

In addition, validation was performed on the test set. Table 3 below shows the confusion matrix and the results of the metrics when recognizing the classifier on the test set.

Table 3. Confusion matrix for classifier based on neural network.

	Basalt Cube	Belgian Cobblestone	Concrete Cube	Cobblestone	Thump	Pothole	Grater
basalt cube	20	0	0	0	0	0	0
Belgian cobblestone	0	20	0	0	0	0	0
concrete cube	0	0	20	0	0	0	0
cobblestone	0	0	0	20	0	0	0
thump	0	0	0	0	20	0	0
pothole	0	0	0	0	0	20	0
grater	0	0	0	0	0	0	20

The provided table indicates that each surface class—basalt cube, Belgian cobblestone, concrete cube, cobblestone, thud, pothole, and grater—was accurately categorized after 20 trials, with no instances of misclassification.

The findings indicate that the neural network operates with high efficiency and precision. Every surface type was categorized with complete accuracy since each category yielded accurate predictions without any mistakes (20 true positives for all categories and 0 false positives or negatives). This indicates that the classifier successfully differentiated each surface type without any ambiguity between classes, which is an optimal outcome for a classification problem.

The increased accuracy indicates that the model effectively processed and identified the distinct characteristics of the surface texture captured throughout the trial. This indicates that the network generalized enough since there were no misclassified instances during validation. The model clearly identified the variations among pavements, including basalt pavement, Belgian pavement, and grating, each possessing unique vibration profiles, and accurately predicted the surface categorization.

The confusion matrix findings indicate that the neural network was efficiently used for the classification job, achieving a high accuracy rate and accurately identifying various surface types without mistakes.

Table 4 presents many performance metrics for the artificial neural network classifier to assess the model's efficacy across distinct surface classifications. The indicated metrics, including sensitivity, specificity, positive and negative predictive values, balanced accuracy, and Area Under the Curve, all possess a value of 1.0000, signifying that the classifier achieved optimal accuracy across all surface categories.

Table 4. Characteristics for classifier based on neural network.

	Basalt Cube	Belgian Cobblestone	Concrete Cube	Cobblestone	Thump	Pothole	Grater
Sensitivity	1.0000	1.0000	1.0000	1.0000	1.0000	1.0000	1.0000
Specificity	1.0000	1.0000	1.0000	1.0000	1.0000	1.0000	1.0000
Pos Pred Value	1.0000	1.0000	1.0000	1.0000	1.0000	1.0000	1.0000
Neg Pred Value	1.0000	1.0000	1.0000	1.0000	1.0000	1.0000	1.0000
Prevalence	0.1429	0.1429	0.1429	0.1429	0.1429	0.1429	0.1429
Detection Rate	0.1429	0.1429	0.1429	0.1429	0.1429	0.1429	0.1429
Detection Prevalence	0.1429	0.1429	0.1429	0.1429	0.1429	0.1429	0.1429
Balanced Accuracy	1.0000	1.0000	1.0000	1.0000	1.0000	1.0000	1.0000
AUC	1.0000	1.0000	1.0000	1.0000	1.0000	1.0000	1.0000

The sensitivity and specificity are both 1.0000, indicating that the model accurately identified both positive (true positive) and negative (true negative) examples without mistake. The neural network successfully classified all surfaces, accurately identifying every positive sample without any false positives.

The positive/negative predicted value is 1.0000, indicating that all predictions provided by the network were accurate. In other terms, each instance the model categorized a surface as a specific class was accurate, and each instance it classed as negative (not belonging to any class) was likewise accurate.

Balanced accuracy is a metric that computes the mean of sensitivity and specificity. As both indicators are at their maximum, the balanced accuracy attains 1.0000, signifying that the model is entirely balanced and precise across all classes. The AUC (Area Under the Curve), which assesses the classifier's capacity to distinguish between classes at various threshold levels, is also at its maximum, signifying optimal classification efficacy.

Collectively, these indications demonstrate that the neural network model operates at optimal efficiency, accurately categorizing each surface type without mistakes, and hence assuring excellent sensitivity, specificity, and accuracy across all classes. This indicates that the model has strong generalization capabilities and exhibits high accuracy across all investigated surface types. The accuracy of prediction on the test set is equal to 100%.

Figure 11 presents the Receiver Operating Characteristics curves for each pavement type estimated for the test set.

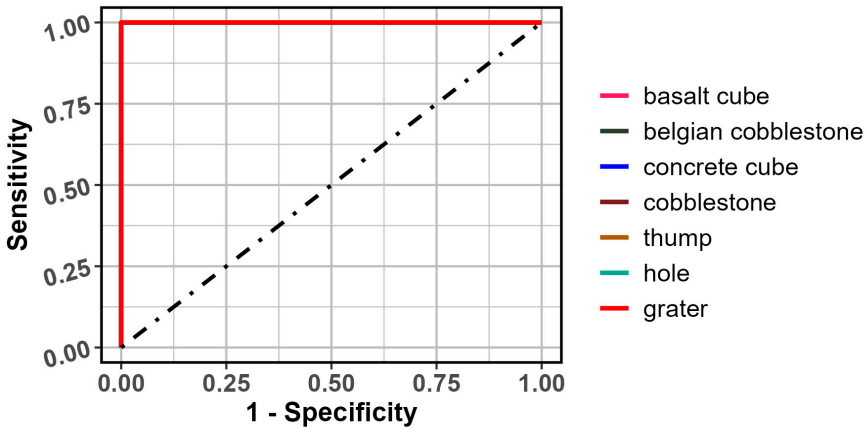

Figure 11. ROC curve for classifier based on beural network.

The ROC curve illustrates the correlation between sensitivity and 1-specificity (the false positive rate) across different classifier thresholds. The illustration illustrates all seven surface types: basalt paver, Belgian paver, concrete tile, stone paver, thud, pit, and grate. Each class ought to possess a distinct curve; nevertheless, this graph illustrates that all the curves converge at the top left corner.

The findings indicate that all surface classes possess an AUC (Area Under the Curve) value of 1.0000, representing the optimal performance metric of the classifier. The model can flawlessly differentiate between all positive and negative instances across all classes, exhibiting no erroneous positive or negative predictions.

The ROC curve's position on the top and left axes indicates that the classifier attains 100% sensitivity (accurately recognizing all positive instances) and 100% specificity (without misclassifying any negative cases), without any trade-offs. This outcome demonstrates that the neural network is exceptionally exact and proficient at identifying all seven surfaces without mistakes. The ROC curve and results indicate that the model is optimal for the surface classification job, as it can flawlessly differentiate all surface types based on their accelerometer data.

4.2. Multinomial Logistic Regression

The parameters of multinomial logistic regression (see Section 2.2) have been estimated. The regularization parameter $\lambda = 0.15$. K-fold cross-validation was used during the learning process. The value of the logarithm of the likelihood function is equal to -570.019. The table below shows the confusion matrix and the results of the metrics when recognizing the classifier on the test set.

This confusion matrix (Table 5) illustrates the outcomes of the multinomial logistic regression classifier. Each row denotes the actual class, while the columns signify the projected class. Optimal predictions should occur only in the diagonal where the actual and projected classes coincide.

The findings indicate that the majority of surfaces were accurately identified; nevertheless, some misclassifications were observed. The model accurately categorized basalt pavement, Belgian pavement, concrete tile, stone pavement, and thud, achieving 20 correct instances in each category, demonstrating its effectiveness in these classifications.

Nonetheless, we see discrepancies in the surfaces of pits and grates. Among the 20 occurrences in the "pit" category, 3 instances were erroneously labeled as "grated", suggesting that the classifier sometimes conflated these two coats. This may result from the similar vibration patterns generated by various coatings, complicating their differentiation.

Furthermore, a sample of the "grating" surface was erroneously identified as "concrete tiles", indicating a minor discrepancy in the prediction of this surface category.

Table 5. Confusion matrix for classifier based on Multinomial Logistic Regression.

	Basalt Cube	Belgian Cobblestone	Concrete Cube	Cobblestone	Thump	Pothole	Grater
basalt cube	20	0	0	0	0	0	0
Belgian cobblestone	0	20	0	0	0	0	0
concrete cube	0	0	20	0	0	0	0
cobblestone	0	0	0	20	0	0	0
thump	0	0	0	0	20	0	0
pothole	0	0	0	3	0	17	0
grater	0	1	0	0	0	0	19

The classifier achieved commendable results, precisely identifying the majority of surfaces. Misclassifications between "pitted" and "grated" coatings indicate that both categories may include similar characteristics that complicate their distinction. The findings indicate that although multinomial logistic regression is an effective methodology, it may struggle to categorize identical signals, necessitating extra data or more advanced techniques to enhance accuracy in these particular categories.

Table 6 displays the performance metrics of the multinomial logistic regression classifier for seven surface categories. The primary metrics encompass sensitivity, specificity, positive and negative predictive values, balanced accuracy, and the Area Under the Curve, which facilitate the assessment of the classifier's proficiency in accurately differentiating between surface types.

Table 6. Confusion matrix for classifier based on Multinomial Logistic Regression.

	Basalt Cube	Belgian Cobblestone	Concrete Cube	Cobblestone	Thump	Pothole	Grater
Sensitivity	1.0000	0.9524	1.0000	0.8696	1.0000	1.0000	1.0000
Specificity	1.0000	1.0000	1.0000	1.0000	1.0000	0.9756	0.9917
Pos Pred Value	1.0000	1.0000	1.0000	1.0000	1.0000	0.8500	0.9500
Neg Pred Value	1.0000	0.9917	1.0000	0.9750	1.0000	1.0000	1.0000
Prevalence	0.1429	0.1500	0.1429	0.1643	0.1429	0.1214	0.1357
Detection Rate	0.1429	0.1429	0.1429	0.1429	0.1429	0.1214	0.1357
Detection Prevalence	0.1429	0.1429	0.1429	0.1429	0.1429	0.1429	0.1429
Balanced Accuracy	1.0000	0.9762	1.0000	0.9348	1.0000	0.9878	0.9959
AUC	1.0000	0.9950	1.0000	1.0000	1.0000	0.9021	0.9838

The findings indicate that the basalt pavement, concrete tile, thud, and grate categories had the highest sensitivity (1.0000), indicating that the model accurately identified all samples of these surfaces. The sensitivities for the Belgian pavement and stone pavement classes were lower, at 0.9524 and 0.8696, respectively. This indicates that certain classes posed more challenges for the model due to some samples being misclassified, as seen in the preceding confusion matrix.

The specificity was very high for all classes, over 1.0000, with the exception of the "pothole" (0.9756) and "grating" (0.9917) surfaces. The model demonstrated proficiency in reliably identifying non-positive instances across several classifications; however, it sometimes erred, particularly in the categorization of "pits" and "grating".

The Positive Predictive Value was uniformly elevated across all categories, attaining a value of 1.0000 in the majority, with the exceptions of the "pit" and "grating" categories, which exhibited somewhat lower values of 0.8500 and 0.9500, respectively. This indicates that the majority of the anticipated positive instances were accurate; nevertheless, the model sometimes misidentified "pits" and "grating" as other surface types.

The AUC, indicating the classifier's capacity to differentiate between positive and negative instances, reached its peak (1.0000) for all categories except for the "pit" (0.9021) and "grating" (0.9838) surfaces. The model exhibited strong performance across most

categories; however, the categorization of "pits" and "grating" surfaces proved to be more challenging.

The multinomial logistic regression model exhibited commendable performance, with high accuracy across the majority of classes; however, the "pit" and "grating" classes were more challenging to discern. This suggests that certain surface types possess similar features to other coatings, resulting in categorization mistakes. The model may be enhanced to more effectively distinguish these surfaces, perhaps by using additional data or more advanced methodologies such as boosted regression trees, random forests. The accuracy of prediction on the test set is equal to 97.14%.

Figure 12 presents the Receiver Operating Characteristics curves for each pavement type estimated for the test set in differentiating among seven distinct surface classes.

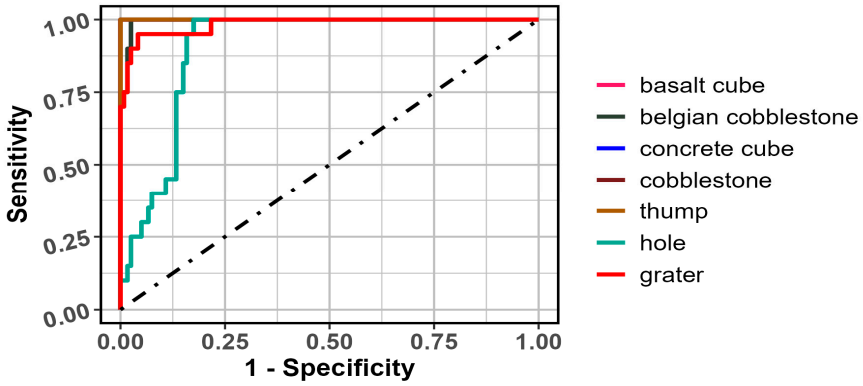

Figure 12. ROC curve for classifier based on multinomial logistic regression.

The findings indicate that the majority of surfaces (basalt pavement, concrete tiles, grating) exhibit an ideal curve that fully conforms to the top and left axes, with a maximum AUC (Area Under the Curve) of 1.0000. The classifier successfully differentiated between the signals of these surfaces, exhibiting neither false positives nor false negatives.

Nonetheless, the separation of some surfaces was not very successful. The curve for the whole class has an elevated incidence of false positives, particularly at the outset, as it diverges from the upper axis and approaches diminished sensitivity at increased specificity values. This suggests that the model had more challenges in precisely differentiating the surface of "potholes" from other surfaces, particularly at lower thresholds. The curves for cobblestone and Belgian cobblestone lag somewhat behind the others; however, they remain around the top axis, indicating competent but imperfect categorization.

The ROC curves indicate that the model proficiently and reliably identified the majority of surfaces, achieving optimal sensitivity and specificity, particularly for basalt pavement, concrete tile, and grating categories. Nevertheless, some classes, such as potholes and stone pavements, posed issues due to their curves exhibiting elevated rates of false positive and negative predictions, signifying the model's struggle to differentiate between these pavements. The model exhibited commendable performance; nonetheless, some classes may require more optimization to achieve enhanced accuracy.

5. Conclusions

1. The experimental results indicated that both classifiers, the neural network and multinomial logistic regression, executed the tasks well. Both models successfully classified the majority of surfaces, attaining a high degree of accuracy and demonstrating a dependable capacity to differentiate among various pavement kinds.
2. The neural network classifier successfully classified all surface types, attaining 100% accuracy on the test set. This illustrates the neural network's exceptional capability to distinguish between pavement kinds based on the generated vibration signals, without any false positives or negatives.

3. The results of the research indicate that the neural network achieved a classification accuracy of 100%, signifying that all surface types were accurately classified without mistake. Simultaneously, the logistic regression model attained an accuracy of 97.14%, although it misidentified certain surfaces, including potholes and uneven pavement. This disparity indicates that the neural network is a superior approach for identifying intricate surfaces, shown by its reduced error rate and a specificity and sensitivity of 1.0000 across all categories.
4. The multinomial logistic regression classifier struggled to accurately identify the 'pothole' cover type, resulting in several misclassifications, especially with the 'graters' class. This indicates that certain surfaces may exhibit similar vibration patterns, complicating precise differentiation.
5. The neural network did not have the same issues as the logistic regression model in accurately categorizing all the "pit" and "grate" surface samples. This reaffirms the advantage of the neural network in classifying these kinds of data.
6. Furthermore, ROC curve research indicated that the AUC (Area Under the Curve) of the neural network was 1.0000 across all surface categories, signifying that the model proficiently differentiated between positive and negative situations. Concurrently, the logistic regression model attained marginally reduced AUC values in some categories, particularly in the 'pit' surfaces, where the AUC reached a mere 0.9021.
7. This categorization may serve as a foundation for the development of sophisticated adaptive suspension controls in vehicles, enabling automated adaptation to varying road conditions, and hence, enhancing driving comfort and safety.

Author Contributions: Conceptualization, V.S., E.K., J.M., P.G., A.L. and A.K.; methodology, V.S., E.K., J.M. and P.G.; software, E.K., J.M., P.G., A.L. and A.K.; validation, V.S., E.K., J.M., P.G., A.L. and A.K.; formal analysis, P.G., A.L. and A.K.; investigation, V.S., E.K. and J.M.; resources, P.G., A.L. and A.K.; data curation, V.S., E.K., J.M., P.G., A.L. and A.K.; writing—original draft preparation, V.S., E.K., J.M., P.G., A.L. and A.K.; writing—review and editing, V.S., E.K., J.M., P.G., A.L. and A.K.; visualization, V.S., E.K. and J.M.; supervision, E.K. and J.M.; project administration, J.M.; funding acquisition, E.K. All authors have read and agreed to the published version of the manuscript.

Funding: This research received no external funding.

Institutional Review Board Statement: Not applicable.

Informed Consent Statement: Not applicable.

Data Availability Statement: Data are available after request.

Acknowledgments: Research was supported by the Joint Research Collaborative Seed Grant Program between National Taipei University of Technology and Vilnius Gediminas Technical University (Grant No: TAIPEI TECH-VGTU-2023-01). This article is the result of Edward Kozlowski's scientific internship that took place at the Vilnius Tech Mechanical Science Institute on 5–28 August 2024.

Conflicts of Interest: The authors declare no conflicts of interest.

References

1. Buczaj, A.; Krzysiak, Z.; Pecyna, A.; Caban, J.; Brumercik, F. Safety during Chemical Transport of Dangerous Goods. *Przem. Chem.* **2019**, *98*, 1276–1280. [CrossRef]
2. Graba, M.; Bieniek, A.; Prażnowski, K.; Hennek, K.; Mamala, J.; Burdzik, R.; Śmieja, M. Analysis of Energy Efficiency and Dynamics during Car Acceleration. *Eksploat. i Niezawodn. Maint. Reliab.* **2023**, *25*, 17. [CrossRef]
3. Maghrour Zefreh, M.; Torok, A. Single Loop Detector Data Validation and Imputation of Missing Data. *Measurement* **2018**, *116*, 193–198. [CrossRef]
4. Surblys, V.; Žuraulis, V.; Sokolovskij, E. Estimation of Road Roughness from Data of On-Vehicle Mounted Sensors. *Eksploat. i Niezawodn. Maint. Reliab.* **2017**, *19*, 369–374. [CrossRef]
5. Žuraulis, V.; Sokolovskij, E.; Matijošius, J. The Opportunities for Establishing the Critical Speed of the Vehicle on Research in Its Lateral Dynamics. *Eksploat. I Niezawodn. Maint. Reliab.* **2013**, *15*, 4, 312–318.
6. Žuraulis, V.; Sokolovskij, E. Vehicle Velocity Relation to Slipping Trajectory Change: An Option for Traffic Accident Reconstruction. *Promet-Traffic Transp.* **2018**, *30*, 395–406. [CrossRef]

7. Kilikevičius, A.; Kilikevičienė, K.; Fursenko, A.; Matijošius, J. The Analysis of Vibration Signals of Critical Points of the Bus Body Frame. *Period. Polytech. Transp. Eng.* **2020**, *48*, 296–304. [CrossRef]
8. Li, X.; Ren, M. Road Adhesion Coefficient Estimation: Physics-Informed Deep Learning Method with Vehicle Dynamics Model. *Expert Syst. Appl.* **2025**, *260*, 125387. [CrossRef]
9. Ulbrich, D.; Selech, J.; Kowalczyk, J.; Jóźwiak, J.; Durczak, K.; Gil, L.; Pieniak, D.; Paczkowska, M.; Przystupa, K. Reliability Analysis for Unrepairable Automotive Components. *Materials* **2021**, *14*, 7014. [CrossRef]
10. Chompooming, K.; Yener, M. The Influence of Roadway Surface Irregularities and Vehicle Deceleration on Bridge Dynamics Using the Method of Lines. *J. Sound Vib.* **1995**, *183*, 567–589. [CrossRef]
11. Maleska, M.; Petry, F.; Fehr, D.; Schuhmann, W.; Böhle, M. Longitudinal Hydroplaning Performance of Passenger Car Tires. *Veh. Syst. Dyn.* **2021**, *59*, 415–432. [CrossRef]
12. Spitzhüttl, F.; Goizet, F.; Unger, T.; Biesse, F. The Real Impact of Full Hydroplaning on Driving Safety. *Accid. Anal. Prev.* **2020**, *138*, 105458. [CrossRef] [PubMed]
13. Ong, G.P.; Fwa, T.F. Modeling and Analysis of Truck Hydroplaning on Highways. *Transp. Res. Rec.* **2008**, *2068*, 99–108. [CrossRef]
14. Cerezo, V.; Gothié, M.; Menissier, M.; Gibrat, T. Hydroplaning Speed and Infrastructure Characteristics. *Proc. Inst. Mech. Eng. Part J J. Eng. Tribol.* **2010**, *224*, 891–898. [CrossRef]
15. Ali, F.; Khan, Z.H.; Khattak, K.S.; Gulliver, T.A. Evaluating the Effect of Road Surface Potholes Using a Microscopic Traffic Model. *Appl. Sci.* **2023**, *13*, 8677. [CrossRef]
16. Khan, Z.H.; Altamimi, A.B.; Imran, W.; Alsaffar, M.; Khattak, K.S.; Alfaisal, F.F. Macroscopic Traffic Modelling on the Impact of Road Surface Potholes: Development and Numerical Solution. *IEEE Access* **2024**, *12*, 81718–81735. [CrossRef]
17. Zhang, Z.; Ren, J.; Ma, J. Incremental Online Non-Parametric Modeling of Surface Vehicle Dynamics Using Adaptive Spectral Metric Gaussian Processes Learning. *Ocean. Eng.* **2024**, *297*, 117117. [CrossRef]
18. Caban, J.; Vrabel, J.; Górnicka, D.; Nowak, R.; Jankiewicz, M.; Matijošius, J.; Palka, M. Overview of Energy Harvesting Technologies Used in Road Vehicles. *Energies* **2023**, *16*, 3787. [CrossRef]
19. Akgol, K.; Gunay, B.; Aydin, M.M. Geometric Optimisation of Chicanes Using Driving Simulator Trajectory Data. *Proc. Inst. Civ. Eng.—Transp.* **2022**, *175*, 238–248. [CrossRef]
20. Aydin, M.M. A New Evaluation Method to Quantify Drivers' Lane Keeping Behaviors on Urban Roads. *Transp. Lett.* **2020**, *12*, 738–749. [CrossRef]
21. Ma, W.; Zeng, L.; An, K. Dynamic Vehicle Routing Problem for Flexible Buses Considering Stochastic Requests. *Transp. Res. Part C Emerg. Technol.* **2023**, *148*, 104030. [CrossRef]
22. Hu, X.; Wei, Y.; Wang, C. Study on Water Entry Impact Characteristics and Parameter Influence Analysis of the Vehicle Passing through the Thin Crushed Ice Zone in a Polar Environment. *Appl. Ocean. Res.* **2024**, *153*, 104250. [CrossRef]
23. Zhang, Z.; Ren, J. Non-Parametric Dynamics Modeling for Unmanned Surface Vehicle Using Spectral Metric Multi-Output Gaussian Processes Learning. *Ocean. Eng.* **2024**, *292*, 116491. [CrossRef]
24. Zeng, Y.; Núñez, A.; Li, Z. Measuring Transfer Functions of Track Structures in a Test Rig with Laser Doppler Vibrometer and Accelerometers on a Moving Vehicle. *Mech. Syst. Signal Process.* **2024**, *214*, 111392. [CrossRef]
25. Gorbunov, M.; Kravchenko, K.; Bureika, G.; Gerlici, J.; Nozhenko, O.; Vaičiūnas, G.; Bučinskas, V.; Steišūnas, S. Estimation of Sand Electrification Influence on Locomotive Wheel/Rail Adhesion Processes. *Eksploat. i Niezawodn. Maint. Reliab.* **2019**, *21*, 460–467. [CrossRef]
26. Boyarchikov, Y.; Martinec, T. Road Pavement Monitoring and Analysis Approaches Using Gyroscope and Accelerometer Data. *IFAC-PapersOnLine* **2024**, *58*, 138–142. [CrossRef]
27. Paziewski, J.; Sieradzki, R.; Rapinski, J.; Tomaszewski, D.; Stepniak, K.; Geng, J.; Li, G. Integrating Low-Cost GNSS and MEMS Accelerometer for Precise Dynamic Displacement Monitoring. *Measurement* **2025**, *242*, 115798. [CrossRef]
28. Ghemari, Z.; Belkhiri, S.; Saad, S. New Parameters for the Capacitive Accelerometer to Reduce Its Measurement Error and Power Consumption. *Meas. Energy* **2024**, *3*, 100018. [CrossRef]
29. Ma, Z.; Han, K.; Choi, J.; Lee, J.; Kwon, O.; Sohn, H.; Liu, J.; Hwang, D.; Aggarwal, J.; Noh, H.; et al. Development and Field Deployment Validation of a Low-Cost and High-Precision Displacement Sensing System by Fusing Millimeter-Wave Radar and Accelerometer. *Eng. Struct.* **2024**, *321*, 118926. [CrossRef]
30. Zhang, M.; Xu, X.; Xu, L.; Ruan, X.; Zhou, D.; He, Z. Fault Diagnosis of Accelerometer Servo Circuit Output Saturation Based on Feature Electrical Parameters Extraction. *Heliyon* **2024**, *10*, e28382. [CrossRef]
31. Lee, S.-K.; Yoo, J.; Lee, C.-H.; An, K.; Yoon, Y.-S.; Lee, J.; Yeom, G.-H.; Hwang, S.-U. Road Type Classification Using Deep Learning for Tire-Pavement Interaction Noise Data in Autonomous Driving Vehicle. *Appl. Acoust.* **2023**, *212*, 109597. [CrossRef]
32. Wu, Y.; Pang, Y.; Zhu, X. Evolution of Prediction Models for Road Surface Irregularity: Trends, Methods and Future. *Constr. Build. Mater.* **2024**, *449*, 138316. [CrossRef]
33. Liang, G.; Zhao, T.; Shangguan, Z.; Li, N.; Wu, M.; Lyu, J.; Du, Y.; Wei, Y. Experimental Study of Road Identification by LSTM with Application to Adaptive Suspension Damping Control. *Mech. Syst. Signal Process.* **2022**, *177*, 109197. [CrossRef]
34. Bystrov, A.; Hoare, E.; Tran, T.-Y.; Clarke, N.; Gashinova, M.; Cherniakov, M. Road Surface Classification Using Automotive Ultrasonic Sensor. *Procedia Eng.* **2016**, *168*, 19–22. [CrossRef]
35. Zhao, T.; He, J.; Lv, J.; Min, D.; Wei, Y. A Comprehensive Implementation of Road Surface Classification for Vehicle Driving Assistance: Dataset, Models, and Deployment. *IEEE Trans. Intell. Transport. Syst.* **2023**, *24*, 8361–8370. [CrossRef]

36. Almotairi, K.H. Hybrid Adaptive Method for Lane Detection of Degraded Road Surface Condition. *J. King Saud Univ.—Comput. Inf. Sci.* **2022**, *34*, 5261–5272. [CrossRef]
37. Hastie, T.; Tibshirani, R.; Friedman, J. *The Elements of Statistical Learning*; Springer Series in Statistics; Springer: New York, NY, USA, 2009; ISBN 978-0-387-84857-0.
38. Géron, A. *Hands-On Machine Learning with Scikit-Learn, Keras, and TensorFlow: Concepts, Tools, and Techniques to Build Intelligent Systems*; O'Reilly Media, Inc.: Newton, MA, USA, 2022; ISBN 978-1-09-812246-1.
39. Rymarczyk, T.; Cieplak, T.; Kłosowski, G.; Kozłowski, E. The Use of LSTM Networks in the Detection of Outliers in IoT- Based Air Quality Monitoring Systems. *Prz. Elektrotechniczny* **2020**, *5*, 91–94.
40. Yan, X.; Su, X. *Linear Regression Analysis: Theory and Computing*; World Scientific Publishing Co. Pte. Ltd.: Singapore, 2009; ISBN 978-981-283-410-2.
41. Rymarczyk, T.; Niderla, K.; Kozłowski, E.; Król, K.; Wyrwisz, J.M.; Skrzypek-Ahmed, S.; Gołąbek, P. Logistic Regression with Wave Preprocessing to Solve Inverse Problem in Industrial Tomography for Technological Process Control. *Energies* **2021**, *14*, 8116. [CrossRef]
42. Kozłowski, E.; Antosz, K.; Sęp, J.; Prucnal, S. Integrating Sensor Systems and Signal Processing for Sustainable Production: Analysis of Cutting Tool Condition. *Electronics* **2023**, *13*, 185. [CrossRef]
43. Kozłowski, E.; Borucka, A.; Świderski, A. Application of the Logistic Regression for Determining Transition Probability Matrix of Operating States in the Transport Systems. *Eksploat. i Niezawodn. Maint. Reliab.* **2020**, *22*, 192–200. [CrossRef]
44. Zou, H.; Hastie, T. Regularization and Variable Selection Via the Elastic Net. *J. R. Stat. Soc. Ser. B Stat. Methodol.* **2005**, *67*, 301–320. [CrossRef]
45. Tibshirani, R. Regression Shrinkage and Selection via the Lasso. *J. R. Stat. Society. Ser. B (Methodol.)* **1996**, *58*, 267–288. [CrossRef]
46. Kozłowski, E.; Borucka, A.; Świderski, A.; Skoczyński, P. Classification Trees in the Assessment of the Road–Railway Accidents Mortality. *Energies* **2021**, *14*, 3462. [CrossRef]
47. Fawcett, T. ROC Graphs with Instance-Varying Costs. *Pattern Recognit. Lett.* **2006**, *27*, 882–891. [CrossRef]
48. James, G.; Witten, D.; Hastie, T.; Tibshirani, R. *An Introduction to Statistical Learning: With Applications in R*, 1st ed.; 2013, Corr. 7th printing 2017 edition; Springer: New York, NY, USA; Heidelberg, Germany; Dordrecht, The Netherland; London, UK, 2013; ISBN 978-1-4614-7137-0.